Heliyon 10 (2024) e35358

Contents lists available at ScienceDirect

Heliyon

journal homepage: www.cell.com/heliyon

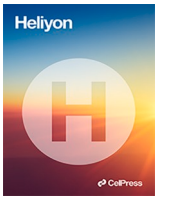

Research article

Geometric feature extraction in nanofiber membrane image based on convolution neural network for surface roughness prediction

Dong Hee Kang [a,b], Na Kyong Kim [c], Wonoh Lee [a], Hyun Wook Kang [a,*]

[a] Department of Mechanical Engineering, Chonnam National University, 77 Youngbong-ro, Buk-Gu, Gwangju, 61186, Republic of Korea
[b] Department of Industrial and Systems Engineering, Texas A&M University, College station, TX, 77843, United States
[c] Green Energy System Research Center, Korea Automotive Technology Institute, 55 Jingoksandanjungang-ro, Gwangsan-Gu, Gwangju, 62465, Republic of Korea

ARTICLE INFO

Keywords:
Convolution neural network
Image preprocessing
Feature extraction
Average surface roughness

ABSTRACT

As a technique in artificial intelligence, a convolution neural network model has been utilized to extract average surface roughness from the geometric characteristics of a membrane image featuring micro- and nanostructures. For surface roughness measurement, e.g. atomic force microscopy and optical profiler, the previous methods have been performed to analyze a porous membrane surface on an interest of region with a few micrometers of the restricted area according to the depth resolution. However, an image from the scanning electron microscope, combined with the feature extraction process, provides clarity on surface roughness for multiple areas with various depth resolutions. Through image preprocessing, the geometric pattern is elucidated by amplifying the disparity in pixel intensity values between the bright and dark regions of the image. The geometric pattern of the binary image and magnitude spectrum confirmed the classification of the surface roughness of images in a categorical scatter plot. A group of cropped images from an original image is used to predict the logarithmic average surface roughness values. The model predicted 4.80 % MAPE for the test dataset. The method of extracting geometric patterns through a feature map-based CNN, combined with a statistical approach, suggests an indirect surface measurement. The process is achieved through a bundle of predicted output data, which helps reduce the randomness error of the structural characteristics. A novel feature extraction approach of CNN with statistical analysis is a valuable method for revealing hidden physical characteristics in surface geometries from irregular pixel patterns in an array of images.

1. Introduction

Surface morphology is one of the critical factors in a porous polymeric membrane that affects membrane performance related to durability [1,2], permeability [3,4], and wettability [5–7]. Analysis of the surface morphology is necessary before developing improvements in the membrane's functioning in various research fields from textile engineering [8–10] to biomedical applications [11–13]. A surface roughness ratio is calculated through the contact area ratio with the sessile droplet to the orthographic projection area. The contact angle of the sessile droplet describes the relative surface energies between the solid surface and the fluids on it. Scanning electron microscope (SEM) image analysis is a typical method to understand the geometries of a porous membrane. In SEM

* Corresponding author.
E-mail address: kanghw@chonnam.ac.kr (H.W. Kang).

https://doi.org/10.1016/j.heliyon.2024.e35358
Received 26 April 2024; Received in revised form 25 July 2024; Accepted 26 July 2024
Available online 27 July 2024

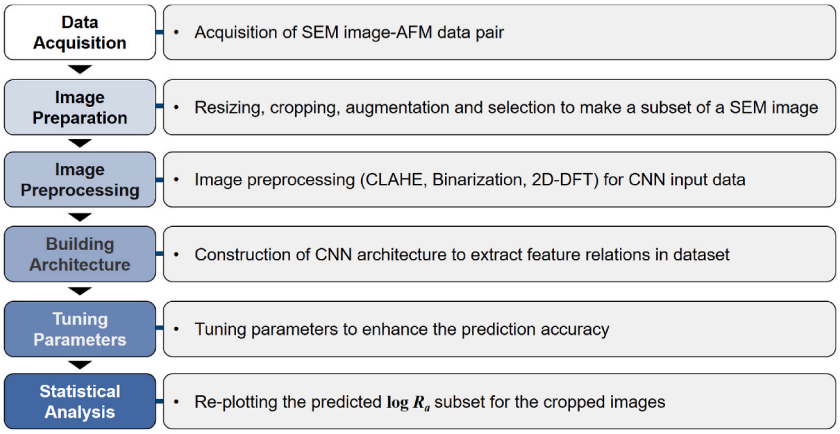

Fig. 1. The flowchart of the geometric feature map-based CNN development.

images, the contrast and brightness difference make a distinction of irregularities in the surface morphology by the image resolution. Extracting features based on the correlation with pixel intensities in the image were attempted to measure the surface roughness [14,15].

A convolutional neural network (CNN) has been designed for image classification tasks to achieve performance on 'human-level' benchmarks [16]. The extraction of critical parameters related to images of the surface characteristics is used in the practical classification work by correlation training in a CNN model, inferring qualitative states into a few noticeable categories. The surface roughness inference model is applied to predict the life expectancy of a target by predicting surface roughness and classifying defect areas from the geometrical pattern of variation of surface characteristics based on the image-surface roughness dataset training [17–19]. Because of the advantages of CNN-based image classification tasks, a non-contact monitoring system has been developed to infer the relation between the surface roughness to estimate the mechanical characteristics [20,21] and evaluate surface quality [22–24]. In particular, the prediction performance of a model using feature extraction from geometric characteristics is limited by the resolution of input data. Bhandari and Park [22] predicted the roughness class on a milling surface via the CNN model to assist in acquiring the preferred machining condition. The milling surface roughness was categorized as fine, smooth, rough, and coarse from the 1–5 μm of roughness range with 93.31 % accuracy for the test data. Zhang et al. [24] evaluated the surface roughness of a grinding surface using an aliasing dispersion index. An aliasing measurement of a surface is reasonable from 0.2 to 0.8 μm of the roughness area with high accuracy above 98.5 %. Li et al. [21] described an online measurement of the surface roughness prediction from laser speckle on cold-rolled strip steel for the 1.0–2.0 μm range. The predicted surface roughness on a material is limited within a range of 1.0 μm [21,23], leading to estimation errors for extrapolation problems as out-of-range predictions. Although these suggested prediction methods have performed well for the target range, they have limitations in extending the prediction domain of surface roughness due to the nature of the input data.

The developed CNN model predicts a logarithmic average surface roughness (log R_a) of a porous polymeric membrane from a group of uniformly cropped SEM images. Preprocessing of the image was feasible for predicting the log R_a, the membrane characteristics with emphasis on geometric patterns are revealed in a feature map. In the CNN model, we attempt to find a consistent pattern that determines the roughness parameter of the membrane surface in multiple cropped images from an original SEM image. A 3-channel layer of each image for input data is displaced to preprocessed images with a contrast-limited adaptive histogram equalization (CLAHE), a binarization, and a two-dimensional discrete Fourier transform (2D-DFT) technique. Predicted values of the log R_a from each cropped image are described as a Gaussian distribution, and it would be used as an alternative approach to image-based quantification of surface characteristics by developing a CNN model to predict physical values from images with geometric patterns. This is the first-time surface roughness for a porous polymer membrane has been predicted through the 3-dimensional CNN, which requires an image and sequential image processing without any tabular data extraction.

2. Experimental

2.1. Data acquisition and preparation

The building of a CNN architecture is performed in sequential steps in Fig. 1 to explore the relationship between the geometric character on an image and its average surface roughness. Two more steps are different from typical CNN methods: image preparation and statistical analysis. A group of cropped images subset from a raw SEM image creates a Gaussian distribution curve, which is composed of their prediction results.

To construct a dataset for the CNN model, we gathered 71 SEM images and their corresponding atomic force microscopy (AFM) results from 25 references [15,25–48]. These SEM images depict nanofiber membranes with an average surface roughness ranging from 5 nm to 6.3 μm. For surface feature prediction on a porous membrane, raw data are obtained from a SEM image paired with an

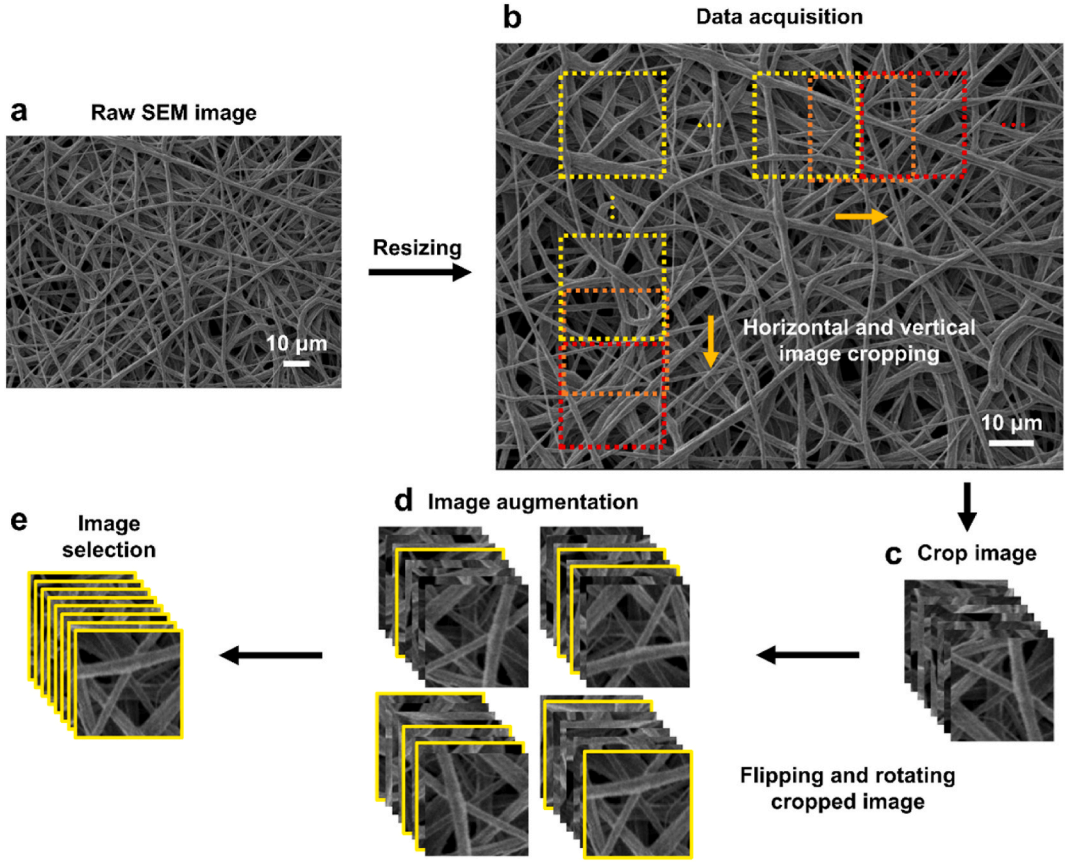

Fig. 2. Image preparation for data acquisition to the input layer of the CNN model. (a, b) Resizing raw SEM image based on the scale bar, (c) Cropping image to 512 × 512 pixels, (d) geometric image augmentation (flipping and rotating), and (e) random selection of 16 images as the one group.

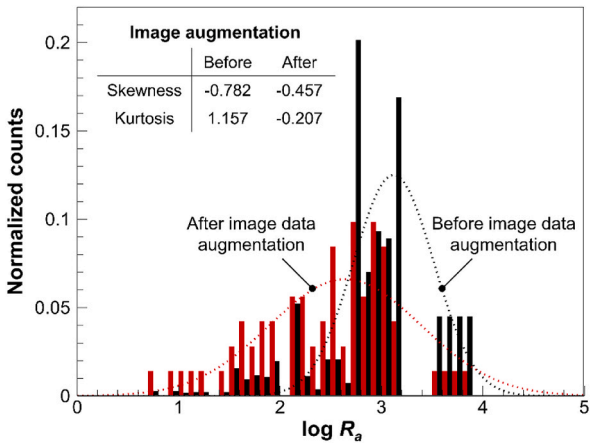

Fig. 3. Distribution of the number of cropped images before and after data augmentation by the log R_a.

average surface roughness (Fig. S1 in the supplemental materials). The input data for the CNN model were obtained through a series of image preparation steps, including image resizing, cropping, augmentation, and selection, as shown in Fig. 2. Initially, all of the raw SEM images with different magnification levels ranging from ×500 to ×30,000 were adjusted to an equivalent magnification ratio. The resizing process reorganized the image size to 51.2 pixels/μm using a respective scale bar of each image. Afterward, the regulated size of SEM image was cropped into multiple images with a size of 256 × 256 pixels size. The cropped images were minimized to less than

Table 1
Architecture of CNN model to predict log R_a from the grayscale images.

Operation Group	Operation	Layer name	Number of filters	Filter size	Output size
Group_0	Input image	Input layer	n/a	n/a	256, 256, 3
Group_1	Convolution (2 times)	Convolution layer	4	3, 3, 4	256, 256, 4
		ReLU layer	n/a	n/a	256, 256, 4
	Pooling	Max pooling layer	1	2, 2	128, 128, 4
Group_2	Convolution (2 times)	Convolution layer	8	3, 3, 8	128, 128, 8
		ReLU layer	n/a	n/a	128, 128, 8
	Pooling	Max pooling layer	1	2, 2	64, 64, 8
Group_3	Convolution (2 times)	Convolution layer	16	3, 3, 16	64, 64, 16
		ReLU layer	n/a	n/a	64, 64, 16
	Pooling	Max pooling layer	1	2, 2	32, 32, 16
Group_4	Convolution (2 times)	Convolution layer	32	3, 3, 32	32, 32, 32
		ReLU layer	n/a	n/a	32, 32, 32
	Pooling	Max pooling layer	1	2, 2	32, 32, 64
Group_5	Convolution (2 times)	Convolution layer	64	3, 3, 64	16, 16, 64
		ReLU layer	n/a	n/a	16, 16, 64
Group_6	Inner product	Flatten	n/a	n/a	16384
		Fully connected layer	n/a	n/a	1024
		ReLU layer	n/a	n/a	1024
	Dropout	Dropout layer (dropout = 0.8)	n/a	n/a	1024
Group_7	Inner product	Fully connected layer	n/a	n/a	1024
		ReLU layer	n/a	n/a	1
	Output	Output layer	n/a	n/a	1

50 % to avoid overlap areas between images (Fig. 2b and c). A cropped image containing text, arrows, or other markings was excluded from the input dataset. The number of cropped images increased by geometric augmentation. Images were rotated 90°, 180°, and 270° and flipped upside down (Fig. 2c and d). After image augmentation, each image group was created with the selected 16 cropped images. Therefore, two cropped images from a raw SEM image were required to create a single image group at least.

The R_a data obtained from AFM analysis on the membrane surface were collected within an area ranging from 1×1 to 75×75 μm^2. The distribution of the R_a data followed an inverse Gaussian distribution within a linear scale range. To enhance prediction accuracy and minimize overfitting, we normalized the input data for the CNN model. The image augmentation process and a log transformation for R_a approximated a normal distribution within the range of surface roughness (Fig. 3). After image augmentation, the skewness and kurtosis of the data distribution approached zero. The wide distribution of log R_a provided sufficient data to improve the prediction accuracy of the CNN model.

2.2. Data preprocessing

Image processing and the construction of a CNN model are performed using the TensorFlow platform within a Python environment. The CNN model analyzes nanofiber membrane images to derive the log R_a by applying convolution and max-pooling operations that extract spatial patterns. All image data is essential for regulating the distribution of gray level intensity, as the contrast and brightness of the SEM images are different depending on the image acquisition environment. Particularly in the preprocessing of low-level images, techniques such as edge sharpening [20] and contrast improvement are employed to extract dominant features from the SEM images by increasing the intensity gradient between adjacent pixels. The pixel intensity gradient contributes to pattern extraction on the convolution and pooling operations. As an image enhancement method, a histogram equalization technique is applied to improve the pixel intensity gradient within the images [49]. Afterward, image transformation is applied to reveal the embedded features in the CLAHE image by converting it through binarization and 2D-DFT processes. The binary image and the 2D-DFT assist in finding a geometric boundary pattern and a periodic pattern in the nanofiber membrane image, respectively. Binarization converts the CLAHE image into a binary image using a process of global fixed thresholding. 2D-DFT extracts periodic patterns in the nanofiber membrane image, revealing spectral characteristics based on the pixel intensity values in the frequency domain of the image [50]. ImageJ software was utilized for image analysis and conversion to grayscale images [51]. The grayscale intensity of the CLAHE image is obtained using ImageJ plugins. Scatter plots are extracted from the binary images by counting the number of isolated black areas and the ratio of white areas. The average and maximum peaks in the magnitude spectrum are determined to be at half-width at half-maximum (HWHM) on the radial profiles.

2.3. Construction of CNN architecture

In general, a CNN assists in looking for correlations between a numerical value in parameter and pixel intensity values in a color image composed of three channels of a two-dimensional array, known as a red, a green, and a blue (RGB) color layer. Convolution operation involves multiplying weights in kernels that slide following the stride over each single channel matrix. Regression analysis validates the architecture's performance in determining correlations between a correct value and a feature map of the convolution layer. The architecture of the developed model is shown in Table 1. After resizing, the input image size to the CNN model has 256 ×

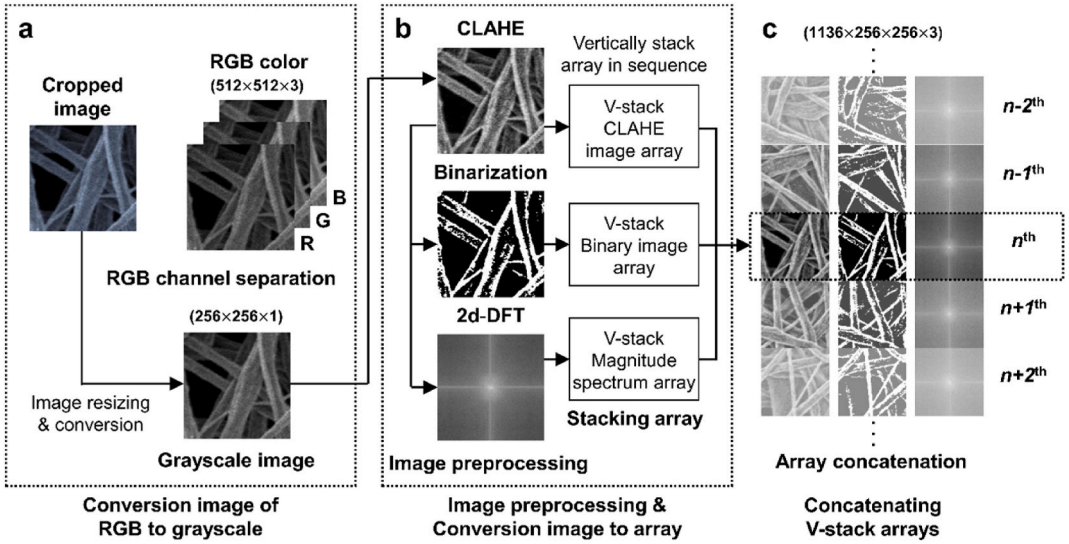

Fig. 4. Image preprocessing and conversion image to array process. (a) Convert RGB color images to grayscale and resize the image. (b) Image preprocessing using CLAHE, binarization, 2D-DFT methods, and conversion to vertical stack array. (c) Concatenating vertically stacked arrays of the CLAHE and binary images and magnitude spectrum. (For interpretation of the references to color in this figure legend, the reader is referred to the Web version of this article.)

256 pixels with 3 channels of grayscale processed images. The images goes through the five operation groups consisting of the convolution layer, rectified linear unit (ReLU) activation layer, and Max-pooling layer, followed by two fully-connected layers. The kernel size of the convolution and the max-pooling layers are 3×3 and 2×2 pixels, respectively. The model is trained using the Adam optimizer to adjust the weights, and the final output layer predicts the value of log R_a. The performance of the developed CNN model is compared with the classic CNN architectures applied to the preprocessed images, namely VGG16 and VGG19 [52], MobileNet [53], Xception [54], ResNet50 [55], and EfficientNetB0 [56]. All fine-tuned CNN architectures are implemented using the Keras open-source software library in Python and are configured to use the ReLU function as activation function for the classifier and to output a single class, with a fine-tuning approach used for optimization. The width and height of input images are scaled to the default input size for each model. The last hidden layer in the VGG16 and VGG19 architectures is reduced to 1/4 (from 4,096 to 1,024 nodes) due to the out-of-memory problem. Key parameters related to the model training and loss function optimization include the learning rate, batch size, and number of epochs. In this case, the Adam optimizer is used with a learning rate of 0.00005. The model is trained with a batch size of 1 and for a total of 100 epochs. These parameters remained the same in all CNN architectures.

2.4. Splitting a dataset

Although the CNN model predicts a single log R_a value from a pixel array of the cropped image, there can be variations in the predicted log R_a values depending on the cropped region of an image due to the irregularity of the membrane surface. The image dataset is divided into training and test datasets to assess the prediction performance. We analyze the average and standard deviation of the log R_a values obtained from a Gaussian distribution of the predicted log R_a values within an image group. The dataset is randomly split into training and test subsets in an 8:2 ratio. When an original image can generate more than 32 cropped images, two image groups are created by randomly selecting the images and separating them into training and test datasets.

2.5. Image conversion to an array for concatenation in the CNN model

To find features at the membrane image for extracting surface roughness, it is required to convert the input layer from an image format to an array of the feature extracted layers. As shown in Fig. 4, the sequential images are organized into three channels within a tensor array: CLAHE image, binary image, and magnitude spectrum. The process begins by converting the RGB color channels of the cropped image into a grayscale image using the average method. Then, data normalization is performed on the image to reduce the difference between images by normalizing the distribution of pixel intensity values, which correspond to the morphological characteristics of the membrane. The measurement environment influences the distribution of the pixel intensity values of an image, such as brightness and contrast involving image resolution. The contrast of image should be regulated by pixel scaling regardless of image quality. Adaptive histogram equalization is performed to improve the pixel intensity value difference in the boundaries of the morphology. Global thresholding and 2D-DFT for a CLAHE image are used to capture inherent patterns related to surface roughness on SEM images. Input data array of a fourth-order tensor concatenates the preprocessed grayscale images in sequence for each channel.

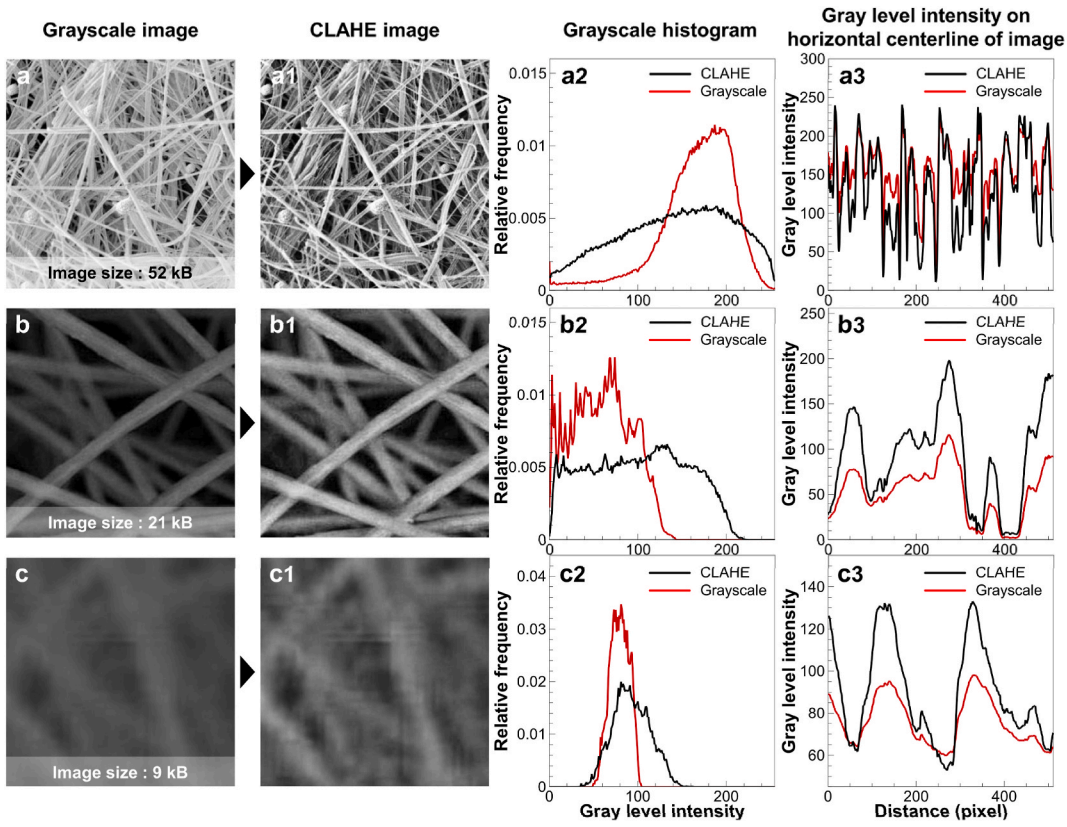

Fig. 5. (a–c1) Image enhancement effect of gray level intensity by CLAHE images compared with grayscale images depending on the image resolution. (a2-c2) Relative frequencies of the gray level intensity. (a3-c3) Gray level intensity on the horizontal line of images.

3. Results and discussions

3.1. Normalization of pixel intensity values on the image

Regardless of the image quality, the borders of the fiber geometry in the image are sharpened through the CLAHE processing, as shown in Fig. 5a–c1. The cropped grayscale images display the highest (52 kB), middle (21 kB), and lowest (9 kB) resolution in the dataset. The grayscale histograms in Fig. 5a2-c2 display the distribution of pixel intensities before and after the CLAHE process. The center of the pixel intensity histogram moves closer to the middle of the grayscale range after the pixel scaling. The difference in the brightness level of an image describes the enhanced pixel intensity gradient at the boundary of geometry. Fig. 5a3-c3 illustrate the horizontal line of gray level intensity from the center of the grayscale images before and after the CLAHE process. The grayscale intensity distribution indicates the bright and dark areas within the image. The intensity peaks of the gray-level scale were obtained from the horizontal center line of the images. The peak-to-peak amplitude rises from 188 to 229, 113 to 193, and 38 to 80 on the highest, middle, and lowest quality images, respectively. The peak-to-peak amplitude increases by 2.67 times for the lowest-resolution image. The enhanced contrast enables better differentiation of depth differences in images. Comparisons between grayscale images and preprocessed images, depending on log R_a values, are described in Table S1 of the supplementary information. Despite the image quality stemming from its inherent resolution, the CLAHE process contributes to enhancing the contrast of pixel intensity in each image, thereby improving the distinction of geometric characteristics between fiber and pore regions. The process aids in the feature extraction of the fiber boundary upon thresholding. The thresholding process enables the classification of the fiber and pore regions of the membrane image. Binarization of the CLAHE images is achieved using global thresholding with a fixed pixel intensity value of 127. In this binary image, a pixel intensity value of 255 corresponds to the fiber area (white), while 0 represents the pore area (black). In addition, another global thresholding method for boundary extraction separates patterns for the periodicity of the brightness difference of the membrane. The separated feature depicts the fiber diameter and directionality in the magnitude spectrum through the 2D-DFT of the CLAHE grayscale image.

3.2. Geometric pattern of pixel intensity values on preprocessing images

A categorical scatter plot in Fig. 6 demonstrates the roughness characteristics, which depend on the ratio of white area to the

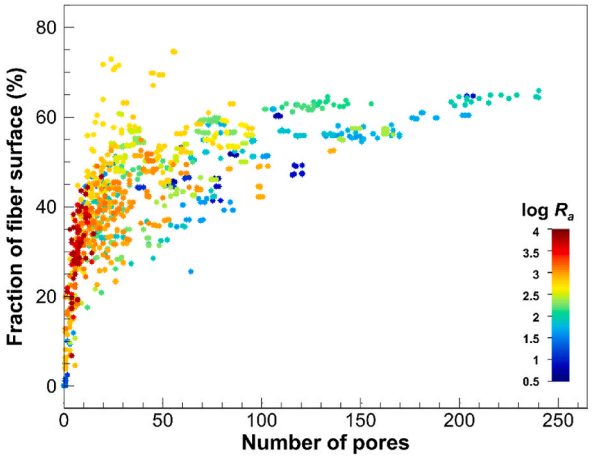

Fig. 6. Binary image analysis depends on the number of the black area isolated on the image and the pixel fraction of the white area.

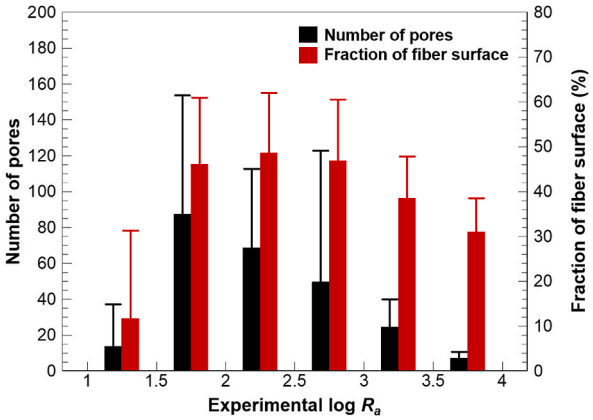

Fig. 7. Feature extraction results of the binary images in the number of pores and a fraction of fiber surface depending on a specific log R_a interval.

number of isolated black areas in the binary image. The geometric boundaries in the binary image can be easily identified by detecting the maximum gradient of pixel intensity values. It allows for the extraction of patterns in the pore and fiber areas during the passage of the kernel in the subsequent convolutional and pooling layers. The scatter plot displays the distribution characteristics of boundary patterns in relation to the diameter and distribution of nanofiber structure in a membrane image. Previous research on membrane roughness has shown a strong positive correlation between the average fiber diameter and the R_a value [14]. Additionally, the fiber fraction in the image and contact angle exhibit a negative and positive correlation, respectively, indicating the hydrophilicity or hydrophobicity of the membrane's surface energy. Fig. 7 presents the average and standard deviation of the feature extraction characteristics on the binary images within specific log R_a intervals. For R_a values higher than 3,000 nm ($\log R_a \geq 3.5$), the number of pores per unit area is 7.4. Due to the number of fibers appearing in the image, the fiber fraction is around 31 %. In the R_a range of 3,000 to 1,000 nm ($3.0 \leq \log R_a < 3.5$), the number of fibers increases as the average fiber diameter decreases, resulting in fewer than 75 pores and a fiber fraction of less than 55 %. Within the R_a range of 1,000–300 nm ($2.5 \leq \log R_a < 3.0$), characteristics extensively appear extensively on the scatter plot, indicating a more uniform fiber diameter distribution. A membrane, which has a wide range of fiber diameter distribution, accounts for a volume fraction of up to 75 %. In the R_a range of 300 to 30 nm ($1.5 \leq \text{lopg } R_a < 2.5$), the membrane is composed of fibers with a small diameter difference of a few tens of nanometers. As the fiber diameter in a membrane decreases, the fiber fraction converges to around 60 %. With an increase in the number of fibers per unit area, the number of pores increases to 250. For R_a values below 30 nm ($\log R_a < 1.5$), the predicted value appears larger than the true value in the scatter plot due to the extrapolation problems when the values are out-of-range. A relatively smooth surface of a membrane, for $\log R_a < 1.5$, exhibits flat features with low pixel gradients. These can resemble images with high surface roughness and wide pores. The boundary identification is unable to distinguish a fiber area with an image resolution of 19.5 nm/pixel in the cropped image. Due to this ambiguous boundary, consistent characteristics in the number of pores and fiber fraction cannot be observed in the scatter plot, making it difficult to clearly recognize patterns at this resolution. According to the pixel intensity for the smooth surface, the fiber fraction in the binary image is classified under 20 %. The region limits the ability to distinguish pixel intensity values at fiber boundaries for feature extraction.

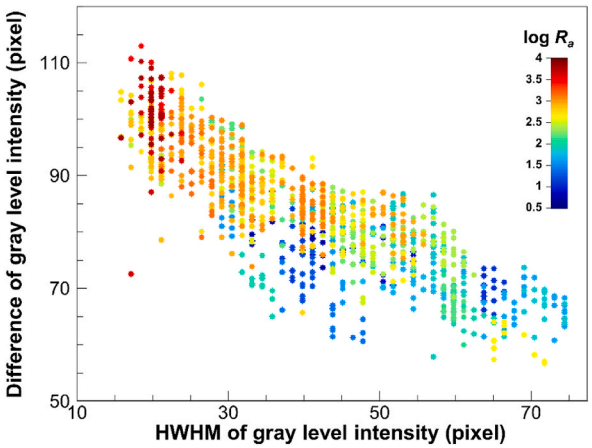

Fig. 8. Magnitude spectrum analysis depends on the half-width at half-maximum of gray level intensity on the radial profile and the maximum difference with the average gray level intensity.

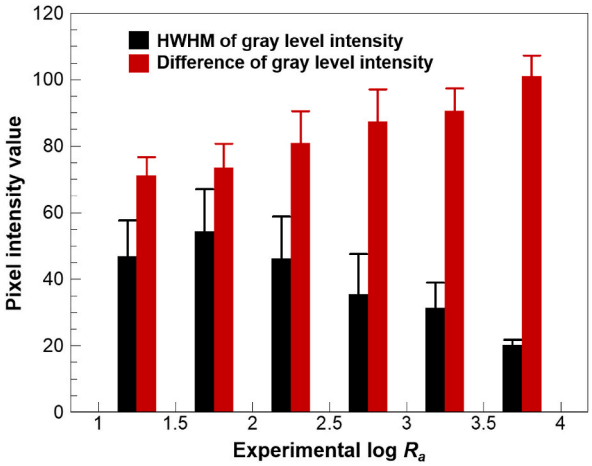

Fig. 9. Feature extraction results in the difference and the HWHM of gray level intensity on the magnitude spectrum depending on a specific log R_a interval.

Furthermore, the 2D-DFT of an image can be used to extract information about the directionality of fibers. The pixel intensity of an image on the spatial coordinates is rearranged in a frequency domain. The grayscale intensity appears along with specific angles in the magnitude spectrum for the fiber direction [57–59]. The result of the magnitude spectrum contains information about the angles at which the fibers appear in the image, and the intensity of the spectrum decreases exponentially from the center to the radial direction. To analyze the magnitude spectrum, a scatter plot is used to display a distribution characteristic of directionality with the diameter of fibers that originate from the difference of gray level intensity in the magnitude spectrum (Fig. 8). The periodic pattern on the magnitude spectrum can be expressed using the HWHM value and the difference between the maximum and average values. In a membrane image, the distribution of pores becomes more uniform as the number of pores increases by decreasing the R_a. The average pixel intensity improves as the gray level intensity increases in the high-frequency component, reducing the difference between the maximum and average gray level intensity. At the magnitude spectrum analysis, the log R_a value has positive and negative relations to the HWHM and the difference of gray level intensities, respectively. Fig. 9 presents the average and standard deviation of the spectral feature characteristics. Transforming an image to a frequency domain through the 2D-DFT is beneficial to describe the periodic pattern for fiber geometries appearing in a nanofiber membrane image. The fiber structures in the high log Ra membrane increase in pixel intensity value differences, where irregular pixel patterns increase the amplitude intensity of the low-frequency component, decreasing the HWHM of the magnitude spectrum. The CLAHE process enhances the contrast at the geometric boundary of a few thick nanofibers with a dark pore region. Therefore, the ratio of a bright region on a low-frequency component is relatively increased, which makes pixel intensity difference between the maximum and the average. In contrast, a nanofiber membrane image with several tens of nm fiber diameters is inadequate to describe the gradient of pixel intensity values in the image. When pixel intensity values are similar to the adjacent pixels in an image (where there is no distinction between fibers and pores on a relatively smooth membrane surface), the high-frequency components increase in the magnitude spectrum. The difference in pixel intensity values between the maximum

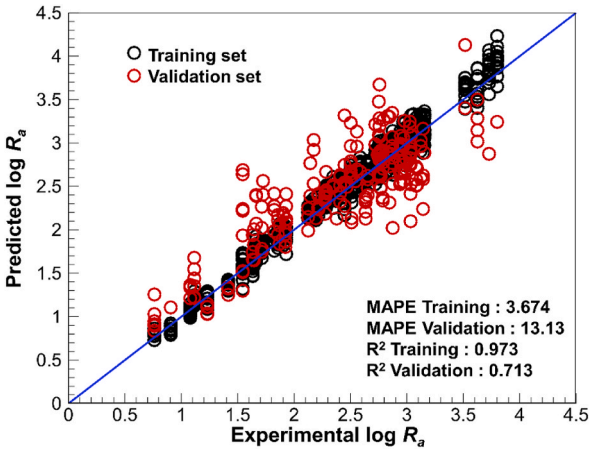

Fig. 10. Prediction values of the log R_a from randomly selected training and validation dataset for optimizing a CNN architecture.

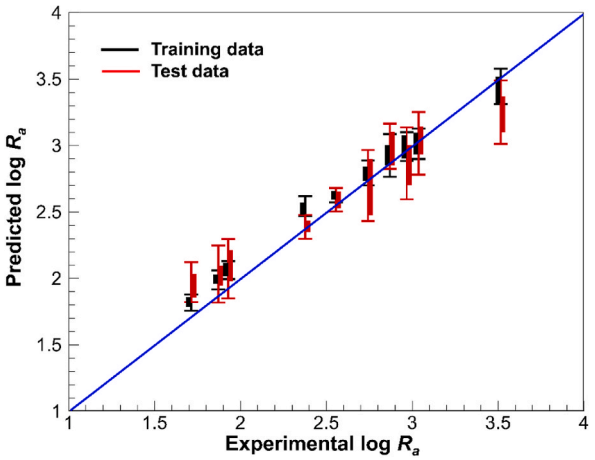

Fig. 11. Predicted log R_a from the selected groups of images for training and test dataset for evaluating predictive performance of the CNN model.

and average values on the magnitude spectrum is reduced. At the same time, the HWHM increases due to the reduction of the low-frequency component. Overall, 2D-DFT preprocessing for a nanofiber membrane image reflects pixel gradients about spectral characteristics of fiber distribution. The variation in surface roughness affects the frequency components.

3.3. Prediction performance to average surface roughness

The prediction results of the optimized architecture of the CNN model are demonstrated using a random subset of cropped images from the training subset. The subset is divided into training and validation subsets in an 8:2 ratio. Fig. 10 shows the Pearson correlation coefficient between the experimental and prediction log R_a values, with the blue line representing the perfect coincidence. Other evaluation indexes, namely the mean absolute percentage error (MAPE) and the coefficient of determination (R^2), are described in the following equations:

$$MAPE = \frac{100\%}{n}\sum_{i=1}^{n}\frac{|y_i - \hat{y}_i|}{y_i}, \tag{1}$$

$$R^2 = 1 - \frac{\sum_{i=1}^{n}|y_i - \hat{y}_i|^2}{\sum_{i=1}^{n}\left|y_i - \bar{y}_{pred}\right|^2}, \tag{2}$$

where y_i, $\hat{y}_i$, and $\bar{y}_{pred}$ represent the experimental value, predicted value, and the average of predicted value, respectively. n is a number of data points. As for the distribution of predictive results in the validation dataset, the number of outliers with lower log R_a than the experimental result occurred as the roughness value increased. The prediction performance for an image with high log R_a is restricted

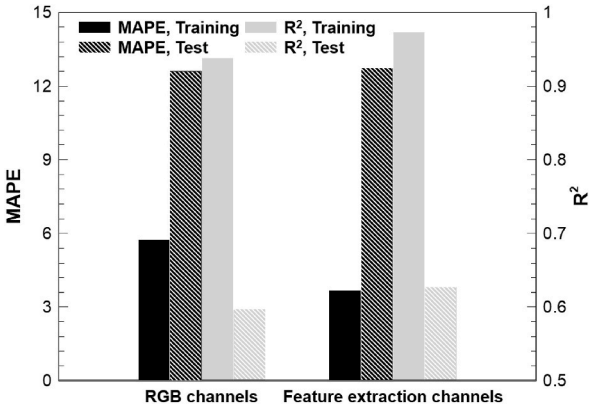

Fig. 12. The MAPE and R^2 of the CNN model evaluation depend on the image channel types for input data.

Table 2
Performance results of the developed CNN model compared with the fine-tuned CNN architectures to the preprocessed images.

CNN Architecture	Depth of model	Total parameters	Inference time (s/step)	MAPE			R^2		
				Train	Validation	Test	Train	Validation	Test
Developed CNN model	12	16.9 M	10.31	3.343	12.874	12.433	0.999	0.979	0.979
VGG16[a] [52]	16	40.4 M	38.62	5.028	8.944	10.251	0.996	0.989	0.983
VGG19[a] [52]	19	45.7 M	47.66	5.354	9.084	10.664	0.996	0.989	0.985
MobileNet [53]	55	3.2 M	17.34	228.839	224.399	132.358	−5.093	−5.462	−2.298
Xception [54]	81	20.9 M	62.76	24.800	31.846	23.456	0.924	0.898	0.932
ResNet50 [55]	107	23.6 M	48.90	46.254	58.753	39.167	0.791	0.690	0.836
EfficientNetB0 [56]	132	4.1 M	48.92	34.065	35.516	30.904	0.886	0.894	0.885

[a] The number of nodes of the last hidden layer (Fully connected layer) is reduced by 1/4 (from 4,096 to 1,024).

to extracting geometric features appearing on a limited image space with a cropped size of 10×10 μm^2. In Fig. 11, which is shown as a boxplot with the Pearson correlation coefficient, artificial classification depending on groups of the image of the input dataset is used to evaluate the prediction performance of the CNN model. The predicted result for training and test data of each image group describes similar correlation characteristics to those predicted by CNN model structure optimization. The evaluation index of the MAPE and R^2 presents decreasing error and increasing relations on a test dataset. The CNN model using the input data with the feature extraction channels showed improved evaluation metrics compared to the model using input data with the raw RGB channels, as shown in Fig. 12.

The prediction performance of the log R_a in the developed model is compared with that of the fine-tuned classic CNN architectures. Table 2 shows the performance results of the developed CNN model and the fine-tuned CNN architectures. Selected CNN architectures from the Keras library were used to compare prediction performance in the order of the number of layers. In particular, compared to the VGG16 and 19 models, despite maintaining high prediction performance, the number of parameters is 58.2 % and 63.0 % smaller, which reduces the inference time to 26.7 % and 21.6 %, respectively. For all the range of log R_a in Table 3, the results of the MAPE and R2 for the developed model are optimized for data training and are similar to the prediction performance of the VGG architectures.

A random subset of cropped images in a group has similar geometric patterns and common characteristics. The results with a Gaussian distribution from the predicted training and test data for each image group are presented in Fig. 13. A blue-dotted line and a number indicate the experimental value of log R_a from AFM at the center of each graph. The Gaussian distribution for each group of dataset prediction results with a statistical approach describes superior prediction accuracy than the prediction result of individual images. Feature extraction from pixel patterns represents the geometric irregularity in an original membrane image, which coincides with a categorical scatter plot. The predicted log R_a at the test dataset, which follows a Gaussian distribution, is similar to the experimental value. The average log R_a for the image groups matches the experimental value, as in Table 4. The MAPE is 4.80 % for the test dataset prediction in the CNN model. The predicted value from an original image matches the result. As a result, the CNN model with multiple images could obtain shared features with high accuracy for the average roughness.

4. Conclusions

A geometric feature map-based CNN model is proposed to predict the average surface roughness of a nanofiber membrane. The feature extraction from the fiber and pore is performed on a tensor of pixels from grayscale images, which are transformed to the spatial and spectral domain after pixel scaling. The irregularity of the nanofiber structure on the membrane surface is represented by the Gaussian distribution of the predicted log R_a, derived from the cropped 16 images. The distribution for the predicted log R_a matches the true value. As the geometric feature difference between cropped images increases, the distribution of log R_a values becomes

Table 3
The MAPE and R^2 results of the developed CNN model and the fine-tuned CNN architectures.

CNN Architecture	MAPE									R^2								
	$0 \leq \log R_a < 2.0$			$2.0 \leq \log R_a < 3.0$			$3.0 \leq \log R_a < 4.0$			$0 \leq \log R_a < 2.0$			$2.0 \leq \log R_a < 3.0$			$3.0 \leq \log R_a < 4.0$		
	Train	Validation	Test	Train	Validation	Test	Train	Validation	Test	Train	Validation	Test	Train	Validation	Test	Train	Validation	Test
Developed CNN model	4.302	20.842	20.469	3.043	8.774	9.944	2.905	11.776	10.781	0.997	0.934	0.919	0.999	0.987	0.984	0.999	0.980	0.984
VGG16[a] [52]	6.351	12.809	16.796	3.949	6.897	6.135	6.336	8.626	11.613	0.994	0.972	0.942	0.998	0.992	0.993	0.995	0.989	0.980
VGG19[a] [52]	9.445	15.237	19.576	3.232	5.779	7.065	5.916	8.751	9.918	0.989	0.967	0.940	0.998	0.994	0.992	0.995	0.987	0.986
MobileNet [53]	479.488	424.550	361.576	171.235	163.233	94.924	55.517	43.086	41.655	−31.413	−30.298	−27.860	−3.626	−3.281	−1.104	0.551	0.726	0.794
Xception [54]	48.021	64.204	45.718	14.734	18.784	17.050	22.306	14.197	18.242	0.714	0.531	0.770	0.962	0.940	0.947	0.923	0.967	0.945
ResNet50 [55]	124.007	153.666	110.861	20.972	19.381	25.521	13.746	10.881	13.311	−0.597	−1.257	−0.340	0.932	0.938	0.894	0.975	0.984	0.974
EfficientNetB0 [56]	67.568	67.483	36.327	17.620	18.551	23.374	35.979	33.016	37.377	0.598	0.633	0.867	0.954	0.950	0.934	0.855	0.876	0.846

[a] The number of nodes of the last hidden layer (Fully connected layer) is reduced by 1/4 (from 4,096 to 1,024).

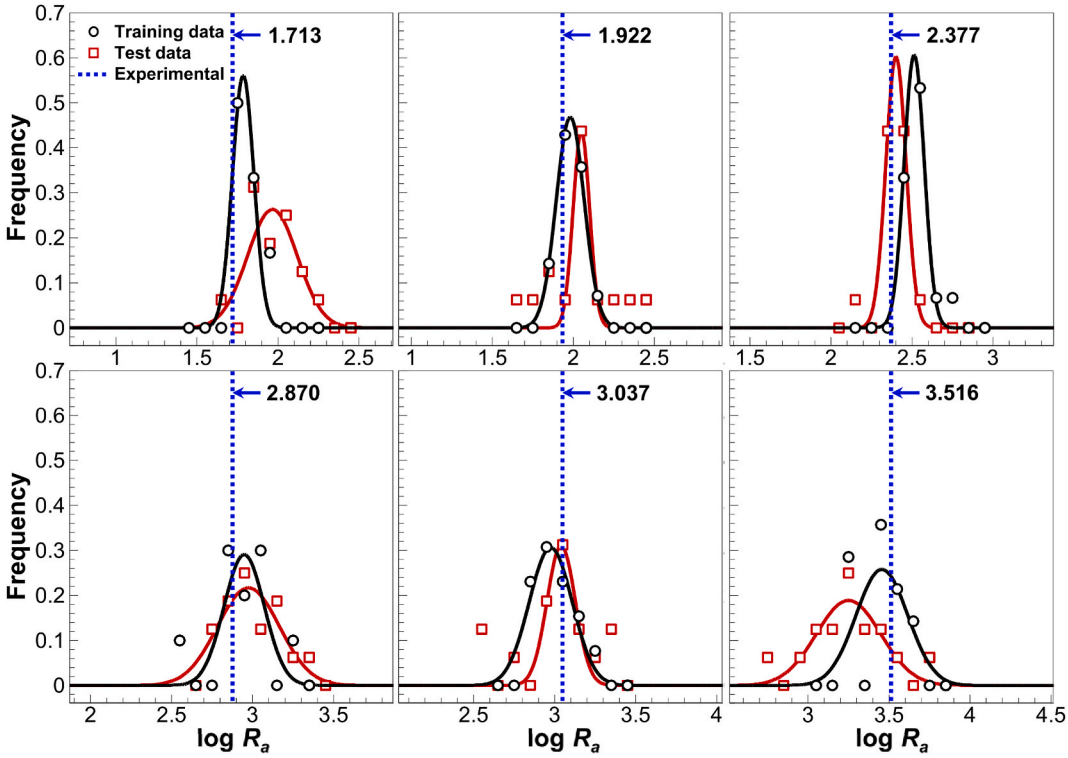

Fig. 13. Comparison of the log R_a obtained from AFM (experimental data) and normalized distributions of the predicted training and test data in each group of images.

Table 4
Prediction results of the log R_a in the selected training and test dataset data groups.

Data group	Experimental data (log R_a)	Training data group (log R_a)	Test data group (log R_a)
1	1.713	1.818 ± 0.061	1.973 ± 0.150
2	1.871	1.989 ± 0.071	2.033 ± 0.215
3	1.922	2.009 ± 0.056	1.900 ± 0.095
4	1.929	2.063 ± 0.068	2.073 ± 0.223
5	2.377	2.545 ± 0.075	2.388 ± 0.090
6	2.556	2.628 ± 0.055	2.593 ± 0.088
7	2.720	2.693 ± 0.083	2.900 ± 0.262
8	2.742	2.795 ± 0.094	2.700 ± 0.267
9	2.751	2.748 ± 0.053	2.847 ± 0.228
10	2.870	2.926 ± 0.161	2.995 ± 0.170
11	2.940	2.926 ± 0.098	2.836 ± 0.258
12	2.968	2.993 ± 0.108	2.867 ± 0.271
13	3.025	3.030 ± 0.055	2.825 ± 0.200
14	3.037	3.014 ± 0.114	3.018 ± 0.236
15	3.516	3.446 ± 0.133	3.252 ± 0.239

broader and deviates from the experimental values. Implementing an algorithm that infers physical meaning from an image is necessary to reveal geometric patterns corresponding to numerical values. After normalization for pixel intensity of images, sequential image preprocessing and conversion to a pixel array are performed to emphasize the geometric feature characteristics of the CNN model. The prediction results for the random subset of cropped images are plotted as a probability density function. It has been confirmed that the average of the Gaussian distribution is close to the true value.

The main contribution of our work can be summarized as follows:

- We integrated three feature maps (CLAHE image, Binary image, and 2D-DFT spectrum) into the CNN model. The geometric feature map-based CNN model predicts the average surface roughness (log R_a) from a group of cropped SEM images of a nanofiber membrane.
- The CLAHE process contributes to data normalization and enhances the contrast of pixel intensity to distinct geometric characteristics. The binarization clarifies to distinguish the fiber and pore region, and the 2D-DFT process reflects pixel gradient about

spectral characteristics of fiber distribution. Categorical scatter plots reveal the relation of the log *Ra* and the pixel distribution for the Binarization and 2D-DFT process.

- A random subset of cropped images for a log R_a prediction with a statistical approach describes superior prediction accuracy than a prediction result of an individual image.
- We verified the prediction accuracy (mean absolute percentage error) and model effectiveness (inference time) of the developed model compared with the classic CNN architectures of VGG16, VGG19, MobileNet, Xception, ResNet50, and EfficientNetB0.

The developed CNN model predicts a wide range of surface roughness values, from 3 μm to 3 nm. The average surface roughness values from a group of cropped images describe a Gaussian distribution. The average of the distribution aligns with the actual surface roughness. However, the feature extraction approach using the magnitude spectrum restricts surfaces without regularity or a material surface where the roughness pattern extends beyond the cropped area. A geometric feature map-based CNN model requires careful architecture design, considering the trade-off between prediction accuracy and inference time for practical applications. Therefore, a different feature extraction strategy and proper architecture construction are needed to evolve the model into a general-purpose tool as a surface roughness prediction across various materials. In conclusion, the sequential image preprocessing for the CNN model and the accompanying statistical analysis of discrete predictive data present a practical approach to artificial intelligence technology. It would be a valuable solution to reveal geometric features and hidden physical characteristics from irregular pixel patterns in an array of images.

Data availability statement

Data have not been deposited into a publicly available repository. Data will be made available on request.

CRediT authorship contribution statement

Dong Hee Kang: Writing – review & editing, Writing – original draft, Validation, Software, Methodology, Investigation, Funding acquisition, Formal analysis, Conceptualization. **Na Kyong Kim:** Writing – review & editing, Validation, Software, Methodology. **Wonoh Lee:** Writing – review & editing, Resources. **Hyun Wook Kang:** Writing – review & editing, Supervision, Resources, Funding acquisition, Conceptualization.

Declaration of competing interest

The authors declare the following financial interests/personal relationships which may be considered as potential competing interests:Hyun Wook Kang reports was provided by Chonnam National University. If there are other authors, they declare that they have no known competing financial interests or personal relationships that could have appeared to influence the work reported in this paper.

Acknowledgements

This work was supported by the National Research Foundation of Korea (NRF) grant funded by the Korea government (MSIT) (No. RS-2023-00211314), the Institute of Information & Communications Technology Planning & Evaluation (IITP) under the Artificial Intelligence Convergence Innovation Human Resources Development (IITP-2023-RS-2023-00256629) grant funded by the Ministry of Science and ICT (MSIT), and the "Regional Innovation Strategy (RIS)" through the National Research Foundation of Korea (NRF) funded by the Ministry of Education (MOE) (2021RIS-002).

Appendix A. Supplementary data

Supplementary data to this article can be found online at https://doi.org/10.1016/j.heliyon.2024.e35358.

References

[1] D. Wong, A. Andriyana, B.C. Ang, E. Verron, Surface morphology and mechanical response of randomly oriented electrospun nanofibrous membrane, Polym. Test. 53 (2016) 108–115, https://doi.org/10.1016/j.polymertesting.2016.05.020.
[2] J. Zuo, T.S. Chung, In-situ cross-linked PVDF membranes with enhanced mechanical durability for vacuum membrane distillation, AIChE J. 62 (2016) 4013–4022, https://doi.org/10.1002/aic.15316.
[3] R.J.F. Kumar, V. Radhakrishnan, P. Haridoss, Enhanced mechanical and electrochemical durability of multistage PTFE treated gas diffusion layers for proton exchange membrane fuel cells, Int. J. Hydrogen Energy 37 (2012) 10830–10835, https://doi.org/10.1016/j.ijhydene.2012.04.092.
[4] P. Zhang, J. Qian, Q. An, X. Liu, Q. Zhao, H. Jin, Surface morphology and pervaporation performance of electric field enhanced multilayer membranes, J. Membr. Sci. 328 (2009) 141–147, https://doi.org/10.1016/j.memsci.2008.11.049.
[5] T.H. Chen, Y.J. Chuang, C.C. Chieng, F.G. Tseng, A wettability switchable surface by microscale surface morphology change, J. Micromech. Microeng. 17 (2007) 489, https://doi.org/10.1088/0960-1317/17/3/010.

[6] D.H. Kang, H.W. Kang, Surface energy characteristics of zeolite embedded PVDF nanofiber films with electrospinning process, Appl. Surf. Sci. 387 (2016) 82–88, https://doi.org/10.1016/j.apsusc.2016.06.096.

[7] J. Zheng, A. He, J. Li, J. Xu, C.C. Han, Studies on the controlled morphology and wettability of polystyrene surfaces by electrospinning or electrospraying, Polymer 47 (2006) 7095–7102, https://doi.org/10.1016/j.polymer.2006.08.019.

[8] H. Wang, L. Chen, Y. Yi, Y. Fu, J. Xiong, N. Li, Durable polyurethane/SiO2 nanofibrous membranes by electrospinning for waterproof and breathable textiles, ACS Appl. Nano Mater. 5 (2022) 10686–10695. https://pubs.acs.org/doi/10.1021/acsanm.2c02017.

[9] A. Yadav, K. Singh, V.K. Shahi, Side-chain grafted functional groups poly (vinylidene fluoride-hexafluoropropylene) anti-fouling fluorinated polymer membrane with tuneable hydrophobicity for distillation, Desalination 525 (2022) 115501, https://doi.org/10.1016/j.desal.2021.115501.

[10] D.H. Kang, N.K. Kim, H.W. Kang, Electrostatic charge retention in PVDF nanofiber-nylon mesh multilayer structure for effective fine particulate matter filtration for face masks, Polymers 13 (2021) 3235, https://doi.org/10.3390/polym13193235.

[11] S.S. Shahriar, A.D. McCarthy, S.M. Andrabi, Y. Su, N.S. Polavoram, J.V. John, M.P. Matis, W. Zhu, J. Xie, Mechanically resilient hybrid aerogels containing fibers of dual-scale sizes and knotty networks for tissue regeneration, Nat. Commun. 15 (2024) 1080, https://doi.org/10.1038/s41467-024-45458-x.

[12] D. Rybak, C. Rinoldi, P. Nakielski, J. Du, M.A.H. Bayan, S.S. Zargarian, M. Pruchniewski, X. Li, B. Strojny-Cieślak, B. Ding, F. Pierini, Injectable and self-healable nano-architectured hydrogel for NIR-light responsive chemo-and photothermal bacterial eradication, J. Mater. Chem. B 12 (2024) 1905–1925, https://doi.org/10.1039/D3TB02693K.

[13] D. Rybak, Y.C. Su, Y. Li, B. Ding, X. Lv, Z. Li, Y. Yeh, P. Nakielski, C. Rinoldi, F. Pierini, J.M. Dodda, Evolution of nanostructured skin patches towards multifunctional wearable platforms for biomedical applications, Nanoscale 15 (2023) 8044–8083, https://doi.org/10.1039/D3NR00807J.

[14] B.H. Moghadam, S. Kasaei, A.K. Haghi, Surface roughness of electrospun nanofibrous mats by a novel image processing technique, Surf. Rev. Lett. 26 (2019) 1830005, https://doi.org/10.1142/S0218625X18300058.

[15] P.K. Szewczyk, D.P. Ura, S. Metwally, J. Knapczyk-Korczak, M. Gajek, M.M. Marzec, A. Bernasik, U. Stachewicz, Roughness and fiber fraction dominated wetting of electrospun fiber-based porous meshes, Polymers 11 (2018) 34, https://doi.org/10.3390/polym11010034.

[16] C. Firestone, Performance vs. competence in human–machine comparisons, Proc. Natl. Acad. Sci. USA 117 (2020) 26562–26571, https://doi.org/10.1073/pnas.1905334117.

[17] Q. Hu, H. Xu, Y. Chang, Surface roughness prediction of aircraft after coating removal based on optical image and deep learning, Sci. Rep. 12 (2022) 19407, https://doi.org/10.1038/s41598-022-24125-5.

[18] C. Knaak, L. Masseling, E. Duong, P. Abels, A. Gillner, Improving build quality in laser powder bed fusion using high dynamic range imaging and model-based reinforcement learning, IEEE Access 9 (2021) 55214–55231, https://doi.org/10.1109/ACCESS.2021.3067302.

[19] P. Wang, Z. Liu, R.X. Gao, Y. Guo, Heterogeneous data-driven hybrid machine learning for tool condition prognosis, CIRP Annals 68 (2019) 455–458, https://doi.org/10.1016/j.cirp.2019.03.007.

[20] J. Ma, T. Wang, G. Li, Q. Zhan, D. Wu, Y. Chang, Y. Xue, Y. Zhang, J. Zuo, Concrete surface roughness measurement method based on edge detection, Vis. Comput. 40 (2024) 1553–1564, https://doi.org/10.1007/s00371-023-02868-0.

[21] S. Li, G. Peng, D. Xu, M. Shao, X. Wang, Q. Yang, A multifeature fusion model for surface roughness measurement of cold-rolled strip steel based on laser speckle, Measurement 227 (2024) 114319, https://doi.org/10.1016/j.measurement.2024.114319.

[22] B. Bhandari, G. Park, Non-contact surface roughness evaluation of milling surface using CNN-deep learning models, Int. J. Comput. Integrated Manuf. 37 (2024) 423–437, https://doi.org/10.1080/0951192X.2022.2126012.

[23] M. Zhao, B. Xue, B. Li, J. Zhu, W. Song, Ensemble learning with support vector machines algorithm for surface roughness prediction in longitudinal vibratory ultrasound-assisted grinding, Precis. Eng. 88 (2024) 382–400, https://doi.org/10.1016/j.precisioneng.2024.02.018.

[24] H. Zhang, Z. Yang, Z. Qiu, B. Chen, Y. Fu, J. Zhan, A visual measurement method of grinding surface roughness based on aliasing region index and neural network, Meas. Sci. Technol. 35 (2024) 055002, https://doi.org/10.1088/1361-6501/ad20c0.

[25] A.A. Abiona, J.A. Ajao, S. Chigome, J.B.K. Kana, G.A. Osinkolu, M. Maaza, Synthesis and characterization of cobalt chloride/poly (ethylene oxide) electrospun hybrid nanofibers, J. Sol. Gel Sci. Technol. 52 (2010) 235–241, https://doi.org/10.1007/s10971-010-2239-0.

[26] F.O. Agyemang, F. Li, F.W. Momade, H. Kim, Effect of poly (ethylene oxide) and water on electrospun poly (vinylidene fluoride) nanofibers with enhanced mechanical properties as pre-filter for oil-in-water filtration, Mater. Chem. Phys. 182 (2016) 208–218, https://doi.org/10.1016/j.matchemphys.2016.07.025.

[27] R.M. Ahmed, Surface characterization and optical study on electrospun nanofibers of PVDF/PAN blends, Fiber Integrated Opt. 36 (2017) 78–90, https://doi.org/10.1080/01468030.2017.1280098.

[28] A. Almasian, N.M. Mahmoodi, M.E. Olya, Tectomer grafted nanofiber: synthesis, characterization and dye removal ability from multicomponent system, J. Ind. Eng. Chem. 32 (2015) 85–98, https://doi.org/10.1016/j.jiec.2015.08.002.

[29] M.B. Chabalala, M.Z. Al-Abri, B.B. Mamba, E.N. Nxumalo, Mechanistic aspects for the enhanced adsorption of bromophenol blue and atrazine over cyclodextrin modified polyacrylonitrile nanofiber membranes, Chem. Eng. Res. Des. 169 (2021) 19–32, https://doi.org/10.1016/j.cherd.2021.02.010.

[30] N. Dorraki, N.N. Safa, M. Jahanfar, H. Ghomi, S.O. Ranaei-Siadat, Surface modification of chitosan/PEO nanofibers by air dielectric barrier discharge plasma for acetylcholinesterase immobilization, Appl. Surf. Sci. 349 (2015) 940–947, https://doi.org/10.1016/j.apsusc.2015.03.118.

[31] M. Faraji, S.R. Nabavi, H. Salimi-Kenari, Fabrication of a PAN–PA6/PANI membrane using dual spinneret electrospinning followed by in situ polymerization for separation of oil-in-water emulsions, New J. Chem. 44 (2020) 13488–13500, https://doi.org/10.1039/D0NJ03231J.

[32] R. Golshaei, Z. Guler Gokce, S.M. Ghoreishi, A. Sezai Sarac, Au/PANA/PVAc and Au/P (ANA-co-CNTA)/PVAc electrospun nanofibers as tyrosinase immobilization supports, Int J Polym Mater Polym Biomat 66 (2017) 658–668, https://doi.org/10.1080/00914037.2016.1252360.

[33] M.I. Hassan, N. Sultana, Characterization, drug loading and antibacterial activity of nanohydroxyapatite/polycaprolactone (nHA/PCL) electrospun membrane, 3 Biotech 7 (2017) 1–9, https://doi.org/10.1007/s13205-017-0889-0.

[34] S.A. Hosseini, M. Vossoughi, N.M. Mahmoodi, Preparation of electrospun affinity membrane and cross flow system for dynamic removal of anionic dye from colored wastewater, Fibers Polym. 18 (2017) 2387–2399, https://doi.org/10.1007/s12221-017-7530-z.

[35] Y. Huang, Q.L. Huang, H. Liu, C.X. Zhang, Y.W. You, N.N. Li, C.F. Xiao, Preparation, characterization, and applications of electrospun ultrafine fibrous PTFE porous membranes, J. Membr. Sci. 523 (2017) 317–326, https://doi.org/10.1016/j.memsci.2016.10.019.

[36] N. Jalalian, S.R. Nabavi, Electrosprayed chitosan nanoparticles decorated on polyamide6 electrospun nanofibers as membrane for Acid Fuchsin dye filtration from water, Surface. Interfac. 21 (2020) 100779, https://doi.org/10.1016/j.surfin.2020.100779.

[37] G. Janani, M.M. Pillai, R. Selvakumar, A. Bhattacharyya, C. Sabarinath, An in vitro 3D model using collagen coated gelatin nanofibers for studying breast cancer metastasis, Biofabrication 9 (2017) 015016, https://doi.org/10.1088/1758-5090/aa5510.

[38] T. Kawano, S. Iikubo, Y. Andou, The relationship between crystal structure and mechanical performance for fabrication of regenerated cellulose film through coagulation conditions, Polymers 13 (2021) 4450, https://doi.org/10.3390/polym13244450.

[39] S.A. Mahmoud, A.A. Al-Dumiri, A.F. Al-Hossainy, Combined experimental and DFT-TDDFT computational studies of doped [PoDA+ PpT/ZrO2]C nanofiber composites and its applications, Vacuum 182 (2020) 109777, https://doi.org/10.1016/j.vacuum.2020.109777.

[40] S.S. Ray, R. Dangayach, Y.N. Kwon, Surface engineering for anti-wetting and antibacterial membrane for enhanced and fouling resistant membrane distillation performance, Chem. Eng. J. 405 (2021) 126702, https://doi.org/10.1016/j.cej.2020.126702.

[41] M. Wang, Y. Cai, B. Zhao, P. Zhu, Time-resolved study of nanomorphology and nanomechanic change of early-stage mineralized electrospun poly (lactic acid) fiber by scanning electron microscopy, Raman spectroscopy and atomic force microscopy, Nanomaterials 7 (2017) 223, https://doi.org/10.3390/nano7080223.

[42] F. Temel, I. Ozaytekin, The monitoring of hydrocarbon vapor by electrospun PBINF modified QCM chemosensor, Sens Actuator A-Phys 326 (2021) 112688, https://doi.org/10.1016/j.sna.2021.112688.

[43] Y. Ting, N. Bunekar, K. Sivasankar, Y.R. Aldori, Using annealing treatment on fabrication ionic liquid-based PVDF films, Coatings 10 (2020) 44, https://doi.org/10.3390/coatings10010044.

[44] P.J. Rivero Fuente, I. Rosagaray Burdaspar, J.P. Fuertes Bonel, J.F. Palacio, R. Rodríguez Trías, Designing multifunctional protective PVC electrospun fibers with tunable properties, Polymers 12 (2020) 2086, https://doi.org/10.3390/polym12092086.

[45] N. Rosman, W.N. Wan Salleh, F. Aziz, A.F. Ismail, Z. Harun, S.S. Bahri, K. Nagai, Electrospun nanofibers embedding ZnO/Ag2CO3/Ag2O heterojunction photocatalyst with enhanced photocatalytic activity, Catalysts 9 (2019) 565, https://doi.org/10.3390/catal9070565.
[46] A. Popelka, A. Abdulkareem, A.A. Mahmoud, M.G. Nassr, M.K.A. Al-Ruweidi, K.J. Mohamoud, M.K. Hussein, M. Lehocky, D. Vesela, P. Humpolíček, P. Kasak, Antimicrobial modification of PLA scaffolds with ascorbic and fumaric acids via plasma treatment, Surf. Coat. Technol. 400 (2020) 126216, https://doi.org/10.1016/j.surfcoat.2020.126216.
[47] H. Morad, M. Jahanshahi, J. Akbari, M. Saeedi, P. Gill, R. Enayatifard, Novel topical and transdermal delivery of colchicine with chitosan based biocomposite nanofiberous system; formulation, optimization, characterization, ex vivo skin deposition/permeation, and anti-melanoma evaluation, Mater. Chem. Phys. 263 (2021) 124381, https://doi.org/10.1016/j.matchemphys.2021.124381.
[48] E. Jahed, M.A. Khaledabad, M.R. Bari, H. Almasi, Effect of cellulose and lignocellulose nanofibers on the properties of Origanum vulgare ssp. gracile essential oil-loaded chitosan films, React. Funct. Polym. 117 (2017) 70–80, https://doi.org/10.1016/j.reactfunctpolym.2017.06.008.
[49] J.A. Stark, Adaptive image contrast enhancement using generalizations of histogram equalization, IEEE Trans. Image Process. 9 (2000) 889–896, https://doi.org/10.1109/83.841534.
[50] C. Ayres, G.L. Bowlin, S.C. Henderson, L. Taylor, J. Shultz, J. Alexander, T.A. Telemeco, D.G. Simpson, Modulation of anisotropy in electrospun tissue-engineering scaffolds: analysis of fiber alignment by the fast Fourier transform, Biomaterials 27 (2006) 5524–5534, https://doi.org/10.1016/j.biomaterials.2006.06.014.
[51] C.A. Schneider, W.S. Rasband, K.W. Eliceiri, NIH Image to ImageJ: 25 years of image analysis, Nat. Methods 9 (2012) 671–675, https://doi.org/10.1038/nmeth.2089.
[52] K. Simonyan, A. Zisserman, Very Deep Convolutional Networks for Large-Scale Image Recognition, 2015 arXiv preprint arXiv:1409.1556.
[53] A.G. Howard, M. Zhu, B. Chen, D. Kalenichenko, W. Wang, T. Weyand, M. Andreetto, H. Adam, Mobilenets: efficient convolutional neural networks for mobile vision applications, arXiv preprint arXiv:1704.04861 (2017).
[54] F. Chollet, Xception: deep learning with depthwise separable convolutions. Proceedings of the IEEE Conference on Computer Vision and Pattern Recognition, 2017, pp. 1251–1258.
[55] K. He, X. Zhang, S. Ren, J. Sun, Deep residual learning for image recognition. Proceedings of the IEEE Conference on Computer Vision and Pattern Recognition, 2016, pp. 770–778.
[56] M. Tan, Q. Le, Efficientnet: rethinking model scaling for convolutional neural networks. International Conference on Machine Learning, PMLR, 2019, pp. 6105–6114.
[57] R. Elashnikov, S. Rimpelová, L. Děkanovský, V. Švorčík, O. Lyutakov, Polypyrrole-coated cellulose nanofibers: influence of orientation, coverage and electrical stimulation on SH-SY5Y behavior, J. Mater. Chem. B 7 (2019) 6500–6507, https://doi.org/10.1039/C9TB01300H.
[58] S.H. Ji, J.S. Yun, Fabrication and characterization of aligned flexible lead-free piezoelectric nanofibers for wearable device applications, Nanomaterials 8 (2018) 206, https://doi.org/10.3390/nano8040206.
[59] B.W. Streeter, J. Xue, Y. Xia, M.E. Davis, Electrospun nanofiber-based patches for the delivery of cardiac progenitor cells, ACS Appl. Mater. Interfaces 11 (2019) 18242–18253, https://doi.org/10.1021/acsami.9b04473.